Correspondence to:
H. Park,
hpark1@ncat.edu

A Sampling-Based Path Planning Algorithm for Improving Observations in Tropical Cyclones

Justice Darko[1] , Larkin Folsom[1], Hyoshin Park[1] , Masashi Minamide[2], Masahiro Ono[3], and Hui Su[3]

[1]Department of Computational Science & Engineering, North Carolina A&T State University, Greensboro, NC, USA, [2]Department of Civil Engineering, The University of Tokyo, Bunkyo-ku, Japan, [3]Jet Propulsion Laboratory, California Institute of Technology, Pasadena, CA, USA

Abstract Lack of high-resolution observations in the inner-core of tropical cyclones remains a key issue when constructing an accurate initial state of the storm structure. The major implication of an improper initial state is the poor predictability of the future state of the storm. The size and associated hazard from strong winds at the inner-core make it impossible to sample this region entirely. However, targeting regions of the inner-core where forecasted atmospheric measurements have high uncertainty can significantly improve the accuracy of measurements for the initial state of the storm. This study provides a scheme for targeted high-resolution observations for small Unmanned Aircraft Systems (sUAS) platforms (e.g., Coyote sUAS) to improve the estimates of the atmospheric measurement in the inner-core structure. The benefit of observation is calculated based on the high-fidelity state-of-the-art hurricane ensemble data assimilation system. Potential locations with the most *informative* measurements are identified through exploration of various simulation-based solutions depending on the state variables (e.g., pressure, temperature, wind speed, relative humidity) and a combined representation of those variables. A sampling-based sUAS path planning algorithm considers energy usage when locating the regions of highly uncertain prediction of measurements, allowing sUAS to maximize the benefit of observation. Robustness analysis of our algorithm for multiple scenarios of sUAS drop and goal locations shows satisfactory performance against benchmark similar to current NOAA field campaign. With optimized sUAS observations, a data assimilation analysis shows significant improvements of up to 4% in the tropical cyclone structure estimates after resolving uncertainties at targeted locations.

1. Introduction

The fundamental understanding of the boundary layer of tropical cyclones (TCs) plays a significant role in providing essential meteorological information. Located between the ocean and atmosphere, the boundary layer contains important information about the inner-core dynamics and requires a true and thorough examination to predict the track and intensity of TCs. An undesirable phenomenon, such as rapid intensification, drives the maximum sustained winds at least 30 kt in a 24 hr period and in particular requires an accurate prediction from an observation of the Planetary Boundary Layer (PBL) in the vicinity of the core (Cione et al., 2013). In recent studies, inner-core observations have been collected with next-generation weather satellites (Zhang et al., 2019). Nonetheless, targeted high-resolution in situ observations using small Unmanned Aircraft System (sUAS) platforms can significantly improve meteorological information (Pillar-Little et al., 2020) about the inner-core and eventually improve the prediction of TC.

The sUAS program (Cione et al., 2016; de Boer et al., 2019; Zhang & Cione, 2021), introduced by the NOAA national hurricane center air reconnaissance programs, well supported the task of monitoring targeted critical layers of a TC. Each sUAS is launched from a tube attached to a P3 hurricane hunter aircraft and controlled remotely from the airplane to be deployed to the lower layer of the PBL, which is extremely dangerous for manned aircraft measurement. However, those existing sUAS deployment has several limitations that can be significantly improved by the proposed observing system. First, the sUAS program has focused on successfully collecting data with drone flight patterns (e.g., eyewall and inflow module) conceived from procedures described in NOAA's Hurricane Research Division Annual Hurricane Field Program. However, these predefined navigation procedures do not necessarily consider how data gathered from a flight path impacts and improves the posterior estimate of the TC at a future time from an earlier prior estimate of the TC. The predefined navigation procedures do not necessarily consider how data gathered from a flight path improves the hurricane forecasting. The criteria for

Validation: Justice Darko
Visualization: Justice Darko
Writing – original draft: Justice Darko,
Hyoshin Park
Writing – review & editing: Larkin
Folsom, Hyoshin Park

location selection were "*difficult to observe in sufficient detail by remote sensing,*" rather than "*optimal observations considering importance of information*" gained from the data in a smaller, more precise target location. Less interest has been shown in regard to how the collected meteorological data would benefit hurricane intensity forecasting by interpolating critical information. A sUAS with its limited endurance and range must consider how traversing a given path, or flight pattern will maximize the resolution of uncertainties in prior TC estimates. For example, in a study by Zhang et al. (2019), uncertainties of forecasted measurements of state variables are estimated by assimilating conventional in situ data and Geostationary Operational Environmental Satellite (GOES)-All-Sky Radiances. These uncertainties can provide background information for targeted high-resolution in situ observations to maximize the removal of uncertainties in the prior estimates of the TC, providing a more accurate approximation for forecasting.

Second, current sUAS program (Cione et al., 2016; de Boer et al., 2019; Zhang & Cione, 2021) does not explicitly consider how the path planning is limited by battery life. This is important for increasing the sample size of critical observations by extending the total distance covered by sUAS, while maintaining the communication with P3 aircraft). For instance, flying at certain angles to the direction of the TC wind velocity will severely impact battery usage. A flight pattern that strives to reduce the energy utilized for navigation will improve the range for in situ observations. The current study seeks to reduce the energy utilized for navigation and improve the distance covered by the sUAS by flying as close as possible with the drift of TC winds. To the best of our knowledge, this is the first study that uses a sampling-based planning algorithm to locate regions of high uncertainties for sUAS along a path to a target location, and overall, improve the efficiency of sUAS battery usage.

2. Related Work

Several environmental and storm-related state variables have been studied to understand the combined impacts on the future structure of TCs. Humidity, absolute vorticity, and distribution of convection relative to the storm were observed to estimate how these variables affect TCs intensification (Munsell et al., 2013; Sippel & Zhang, 2008, 2010). In addition, aircraft observations of upper-ocean thermal structures show that there is a strong correlation between the upper-ocean thermal variability and the intensity change of TCs (Sanabia et al., 2013). Other studies have also demonstrated a strong relationship between the measurement of the central pressure of TC and its maximum sustained winds speed (Rosendal & Shaw, 1982).

The sensitivity of TCs forecasting to the quality of atmospheric data has received significant attention (Raavi & Walsh, 2020). NOAA's current field campaigns seek to assimilate high-resolution in situ observations in the inner-core region from the sUAS platform (Cione et al., 2016; de Boer et al., 2019; Zhang & Cione, 2021). The campaigns allowed the National Hurricane Center (NHC) to measure critical variables and parameters in the PBL. The accuracy of data collected by the sUAS agreed well or sometimes capturing more variability than the manned measurement (Cione et al., 2013, 2020). While NOAA continues to deploy sUAS in TCs, locations are not optimized but limited to predefined navigation schemes, which do not consider the benefit of observing the target location. In this paper, sUAS Navigation schemes have more benefits for TC forecasting by identifying a better location to target be estimating the uncertainties of prior measurements. A review of continuous monitoring of a TCs' core using sUAS is provided in (Tyrrell & Holland, 2003).

The impact of the internal dynamics on TC intensification and structural changes revealed that hybrid data assimilation techniques improved the overall quality of prediction compared to individual data assimilation methods (Malakar et al., 2020). A flow-dependent sequential assimilation-based targeted observation using the ensemble Kalman filter could minimize the analysis variance (Wu et al., 2020). Data assimilation experiments show how sUAS data can be used to improve storm structure analysis (Cione et al., 2020). Prediction accuracy of TCs in both coupled dynamical and statistical models was improved by successful observation and assimilation of upper-ocean temperature (Sanabia et al., 2013). Table 1 summarizes common observational parameters that have been collected and assimilated for the accurate prediction of TC structure. This study estimates the actual improvement over the posterior measurement achieved with sUAS observation through a data assimilation analysis equivalent to a simple scalar illustration of the least squares prior estimation.

The remainder of this paper's structure is as follows: Section 3 describes the sampling-based path planning method, development of a combined measure of uncertainty, and a presentation of a constraint for safe and energy-efficient navigation. In Section 4, we present an evaluation of the model performance and test its robustness through

Table 1
Summary of TC Prediction Parameters of Interest

Parameters	Target	Observational equipment	Forecast	Previous studies (examples)
Wind speed, wind direction	Eye, eyewall, inflow, PBL	Reconnaissance aircrafts (>2 km), Buoys (SST), UAS (<2 km), Dropsonde	Intensity, structure	Rosendal and Shaw (1982), Cione et al. (2020), Stern et al. (2016), DeMaria and Kaplan (1999), and DeMaria et al. (2005, 2014)
Air temperature, SST	PBL, inflow, upper-ocean layers		Intensity, structure, track	Sanabia et al. (2013), Zhang et al. (2017), Cione et al. (2020), Stern et al. (2016), DeMaria and Kaplan (1999), and DeMaria et al. (2005, 2014)
Pressure	Eye, eyewall, inflow, PBL	Reconnaissance aircrafts (>2 km), UAS (<2 km), Dropsonde		Rosendal and Shaw (1982), Goyal and Datta (2011), Zhang et al. (2017), Cione et al. (2020), Stern et al. (2016), DeMaria and Kaplan (1999), and DeMaria et al. (2005, 2014)
Moisture (RH)	Eyewall, inflow, PBL		Intensity, structure	Sippel and Zhang (2008, 2010), Munsell et al. (2013), Van Sang et al. (2008), Zhang et al. (2017), Cione et al. (2020), Stern et al. (2016), DeMaria and Kaplan (1999), and DeMaria et al. (2005, 2014)
TKE momentum flux	Eyewall, inflow, PBL (<150 m)	UAS (<2 km) Dropsondes	Intensity, structure	Cione et al. (2020), Stern et al. (2016), and Pillar-Little et al. (2020)

Note. PBL, planetary boundary layer; RH, relative humidity; SST, sea surface temperature; TKE, turbulence kinetic energy.

a Monte Carlo simulation. Section 5 presents an illustration of a typical sUAS mission utilizing the proposed deployment scheme, with data assimilation analysis to estimate improvement levels. Finally, a summary of the study's findings and future research direction is presented in Section 6.

3. Model, Data, and Methods

The wind velocities play a major role in describing the highly dynamic environment of a TC configuration space. To provide safer maneuverability for sUAS in such environments, a rapidly exploring random tree star (RRT*) algorithm, previously applied to Mars (Folsom et al., 2021), is revised in this study, which converges to collision-free and efficient path solutions. RRT* algorithm starts by growing a tree that includes the initial dropoff location of the sUAS as its single vertex and no edges. The algorithm then incrementally grows a tree on the TC configuration space by randomly sampling a location within the space and extending the tree to that location. This study uses the RRT* algorithm to simulate the sUASs' flight for targeting locations of TCs where prior predictions of measurements have large uncertainty. The benefit of a solution is estimated by computing the difference between before and after in situ sUAS observations at a target location. In this study, we consider four atmospheric state variables consistent with sUAS sensor payload for measuring pressure, temperature, wind speed, and relative humidity. Since sUAS will always have all these atmospheric measurements on hand, these state variables are linearly combined to show different, a combined representation of the uncertainties in TC forecasting. The combined representation of uncertainty $\sigma_{C(i)}$ at location i in the TC's configuration space is written as:

$$\sigma_{C(i)} = \sum_{x \in X} w_x \sigma'_{(x,i)} \tag{1}$$

where $x \in X$ is the set of state variables (i.e., pressure, temperature, wind speed, and relative humidity), $\sigma'_{(x,i)}$ are the normalized uncertainties of the prior forecasted measurement for state variables $x \in X$, and w_x, are the weights for the state variable uncertainty in the TC space. The normalized uncertainties ensure that the values of uncertainty for the state variables are within the same range, whereas the weights determine the importance of the uncertainty of each variable in the combined representation. While optimal weight assignment, partial-correlation,

and nonlinearity between state variables are outside the scope of this study, the future research can improve the TC forecasting performance by considering these aspects. For example, path solutions may have higher improvements in TC forecast accuracy if a larger weight is assigned to uncertainties of relative humidity compared to the other variables, considering an immediate impact of inner-core moisture on forecast errors (Emanuel & Zhang, 2017).

The normalized uncertainties $\sigma'_{(x,i)}$ for the prior forecasted measurement of each state variable x at location i is written as:

$$\sigma'_{(x,i)} = \frac{\sigma_{P(x,i)} - \sigma_{P(x,\min)}}{\sigma_{P(x,\max)} - \sigma_{P(x,\min)}}, \tag{2}$$

where $\sigma_{P(x,\min)}$ and $\sigma_{P(x,\max)}$ are minimum and maximum uncertainty for the prior forecasted measurement of state variable x, and $\sigma_{P(x,i)}$ is the uncertainty for prior forecasted measurement of variable x at location i. The sum of weights for the uncertainties of the state variable is equal to one:

$$\sum_{x \in X} w_x = 1 \tag{3}$$

3.1. TC STRAP-RRT*

We call the developed extension of the RRT* algorithm as *S*uas naviga*T*ion with en-*R*oute measurement *A*ccumulation *P*lan (STRAP). The main objective is to find nodes that lower the overall energy for a given path while maximizing the uncertainty removal along the path from a start to a target location. Since strong flow fields in TC usually have ambient flow speed greater than sUAS speed relative to the flow; some paths prevent sUAS from progressing forward relative to a ground-fixed and rotating reference frame. Although this paper will present a specific TC sUAS deployment scenario for an illustration of STRAP-RRT*, this algorithm is flexible to adapt to different environments in scale, eyewall structure, and P3 aircraft deployment strategy:

1. This algorithm ensures path feasibility and minimal energy utilization for navigation in the strong winds of TC by considering the direction of the TC wind vector and the RRT* path segment in a wind velocity constraint for the path solution. The size of each measurement can be mapped in a grid cell and the size of the cell is scalable. As shown in previous research (Folsom et al., 2021), the developed RRT* is scalable to different size of the network

2. Because we consider the direction of the TC wind vector for generating feasible paths, we expect the algorithm to easily adapt to different eyewall structures (i.e., annular and polygonal) by following the wind flow pattern of the eyewall. Sometimes the size of the eye will be an issue for P3 aircraft to loiter around the sUAS to receive collected data, however, with the improved range of the communication, this can be resolved in the future deployment

3. The simultaneous and sequential sUAS platforms launched from P3 will show different path. Although this paper presents a single sUAS platform, the future study can estimate the benefit of observation; a simultaneous launch will benefit from highly informative small areas with optimal formation of sUAS, while a sequential launch will benefit from sparse information in large areas with adaptation to new information

Given the RRT* path segment $\bar{a}_i$ and TC wind vector $\bar{b}_i$ at location i in TC configuration space, the angle θ between $\bar{a}_i$ and $\bar{b}_i$ is calculated as

$$\theta = \arccos\left(\frac{\bar{a}_i \cdot \bar{b}_i}{|\bar{a}_i| \cdot |\bar{b}_i|}\right) \tag{4}$$

The wind velocity constraint is implemented as the maximum angular difference that is acceptable between a sub-path segment of the RRT* tree and the wind direction at location i. In this study, the maximum difference Θ is set at less or equal to $50°$, to allow some room to navigate around the direction of the wind. The set of all sUAS waypoints in the optimal path solution will satisfy the constraint $\theta \leq \Theta$. An end result of the wind velocity constraint is an increased range of coverage by the sUAS for the same endurance. The speed of the sUAS relative to a fixed point on the earth's surface (ocean) is the ground speed (Figure 1).
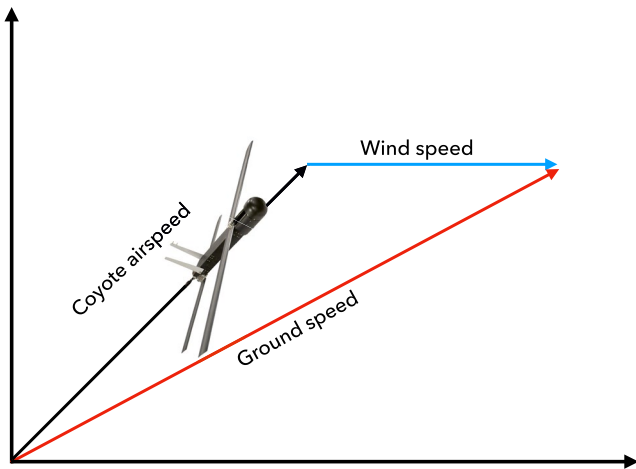
Figure 1. sUAS ground speed representation.

The velocity of the sUAS is thus given as the vector sum of the sUAS airspeed and the TC wind, written as:

$$\bar{V}_{Ground} = \bar{V}_{sUAS} + \bar{V}_{Wind} \tag{5}$$

It can be seen from Equation 5 that the relative speed of the sUAS to the ocean is higher than the sUAS airspeed. In scenarios where the angular difference between the sUAS and wind is zero, the speed of the sUAS relative to the ocean will be the sum of the TC wind and sUAS's speed. This important deduction is developed as a result of the wind velocity constraint.

For an illustration of STRAP-RRT* algorithm (Figure 2), we first extend a nearest-neighbor vertex toward a randomly sampled location in the TC configuration space. The extension process creates a new vertex q_{new}, at a distance less than or equal to a defined step size. The algorithm then connects q_{new} to the vertex that incurs the maximum total uncertainty $\left(\sum \sigma_C\right)$ from our start location within the set of vertices found in a defined vicinity around q_{new} (parent stage). STRAP-RRT* also reevaluates previous connections and extends the new vertex to the vertex that can be accessed through the maximum uncertainty, described as the rewire stage. At the point of rewiring, the algorithm searches among all existing nodes within the defined vicinity of q_{new}.

As shown in the pseudocode (Algorithm 1), the Nearest function in STRAP-RRT* (NearestSTRAP) considers the uncertainty at the nearest node. NoExceed conditional statement implements the wind velocity constraint. The ChooseParent function considers the closest node by uncertainty, rather than distance.

4. Model Evaluation

This section provides an evaluation of the model for different random scenarios. Optimal sampling of uncertainties for thermodynamic (e.g., pressure, temperature, and relative humidity) and kinematic (e.g., wind speed) measurements are performed using the modified sampling-based planning algorithm STRAP-RRT*. We compare this to a benchmark approach, the minimum distance method (MDM) subject to the wind velocity constraint. The main objective of the MDM is to make observations along a minimum circumnavigation path between a start
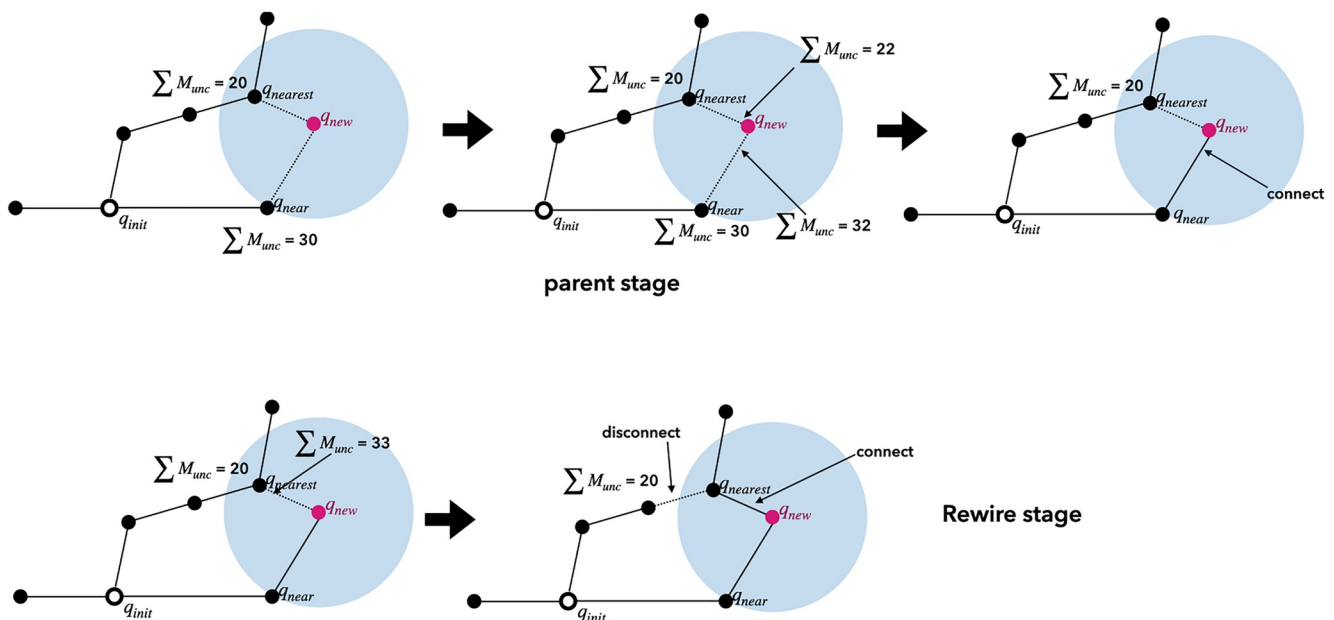

Figure 2. Stages of RRT* for exploring TC space.

Algorithm 1. STRAP-RRT*

T ← InitializeTree()

T ← InsertNode(∅, z_{init},T)

for $i = 0$ to i = N **do**

      z_{rand} ← Sample(i)

      $z_{nearest}$ ← NearestSTRAP(T,z_{rand})

      (z_{new}, U_{new}) ← Steer($z_{nearest}$, z_{rand})

      if NoExceed(z_{new}) **then**

            z_{near} ← Near(T, z_{new}, |V|)

            z_{max} ← ChooseParentSTRAP(z_{near}, $z_{nearest}$, z_{new})

            T← InsertNode(z_{max}, z_{new}, T)

            T← Rewire(T, z_{near}, z_{max}, z_{new})

    end if

end for

---

and goal location. This MDM method is similar to the circumnavigation procedure used in the "eyewall" module of sUAS deployment in the current NOAA field campaigns (Cione et al., 2020).

In this study of in situ sUAS observation platform, we adopt the Coyote sUAS that was previously used in NOAA's hurricane field campaigns. As demonstrated by Cione et al. (2020), in situ Coyote sUAS observations were usually made at a constant altitude; thus, this study assumes a level flight for the in situ Coyote observations. A typical Coyote sUAS battery life supports 3,600 s endurance, shorter if in a highly turbulent environment. At a maximum cruising airspeed of 36 m s^{-1} (Cione et al., 2016), the total distance that can be covered by Coyote sUAS assuming battery life of 3,600 s is 80 mi. This distance is significantly increased when the wind velocity constraint is factored in. To transmit data in near-real-time during observations, Coyote sUAS are equipped with a 350 MHz data link that improves the communication range of the Coyote substantially and allows the P3 hurricane hunter aircraft to execute normal flight paths while Coyote sUAS navigates its path.

4.1. Preliminary Analysis of Uncertainty Distribution

The uncertainty distribution of the prior forecasted measurements for Hurricane Harvey is used in this study. The uncertainties are represented by the ensemble spread and calculated as the forecasted measurements' standard deviation. To generate the uncertainty distribution for Hurricane Harvey, conventional in situ observations (e.g., Dropsondes) and all-sky satellite radiance from GOES-16 were assimilated in a state-of-the-art data assimilation system (ensemble Kalman filter (EnKF); Minamide et al., 2020; Zhang et al., 2019). The data assimilation system was developed at the Pennsylvania State University and built around the Advanced Weather Research and Forecasting Model (WRF-ARW) and the Community Radiative Transfer Model (CRTM) to provide hourly temporal resolution forecast of Hurricanes.

We use the uncertainty distributions of a one-hour (1-hr) forecast window at 00:00 UTC August 25 for four state variables (Figures 3a–3d), and their combined representation using Equation 1 (Figure 3d) in the storm-centered horizontal cross sections at a 1.1-km level, for three reasons. First, the TC vortex position is relatively fixed and has minimal position uncertainty in short time intervals (typically 1-hr; Poterjoy & Zhang, 2011), which is similar to the battery life of Coyote sUAS in this study. Although the STRAP-RRT* can be recalculated in an online fashion in communication with P3 aircraft and new flight paths can be calculated on the fly, this paper investigates the benefit of fixed-path sUAS observation in TC forecasting. A larger forecast window can easily lead to mission failure if the TC vortex position changes. It is, therefore, reasonable to use our algorithm on shorter time windows where the position of the vortex is relatively fixed. Implementing the algorithm on larger forecast windows will require modifications to adapt to the TC vortex position changes. Second, considering this specific case of Coyote sUAS with an endurance of approximately 1-hr, it is appropriate to implement the path planning algorithm for a 1-hr forecast window. For sUAS's with higher endurances, the path planning algorithm can be modified the larger forecast window. Finally, our choice of 00:00 UTC August 25 is to highlight the improvement in TC forecasting
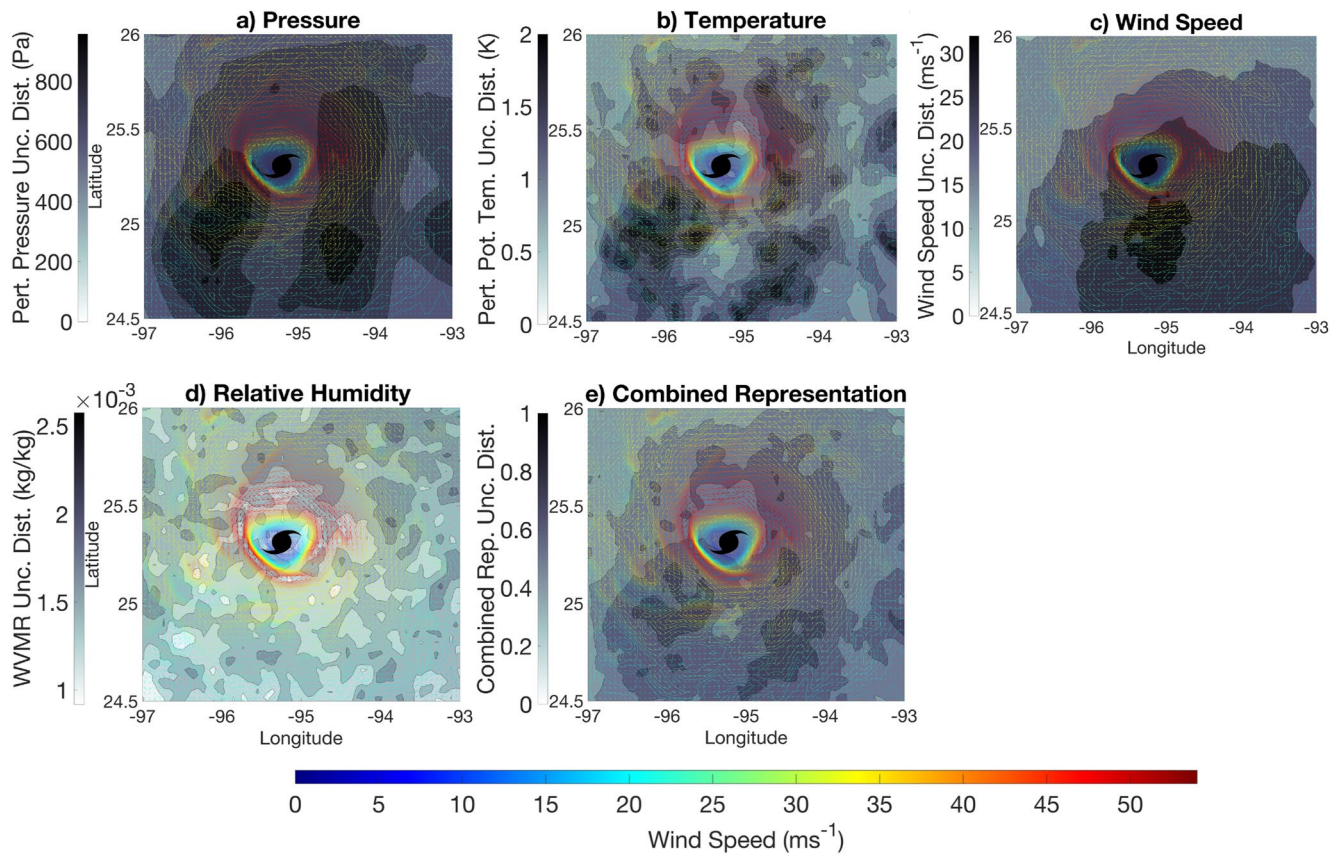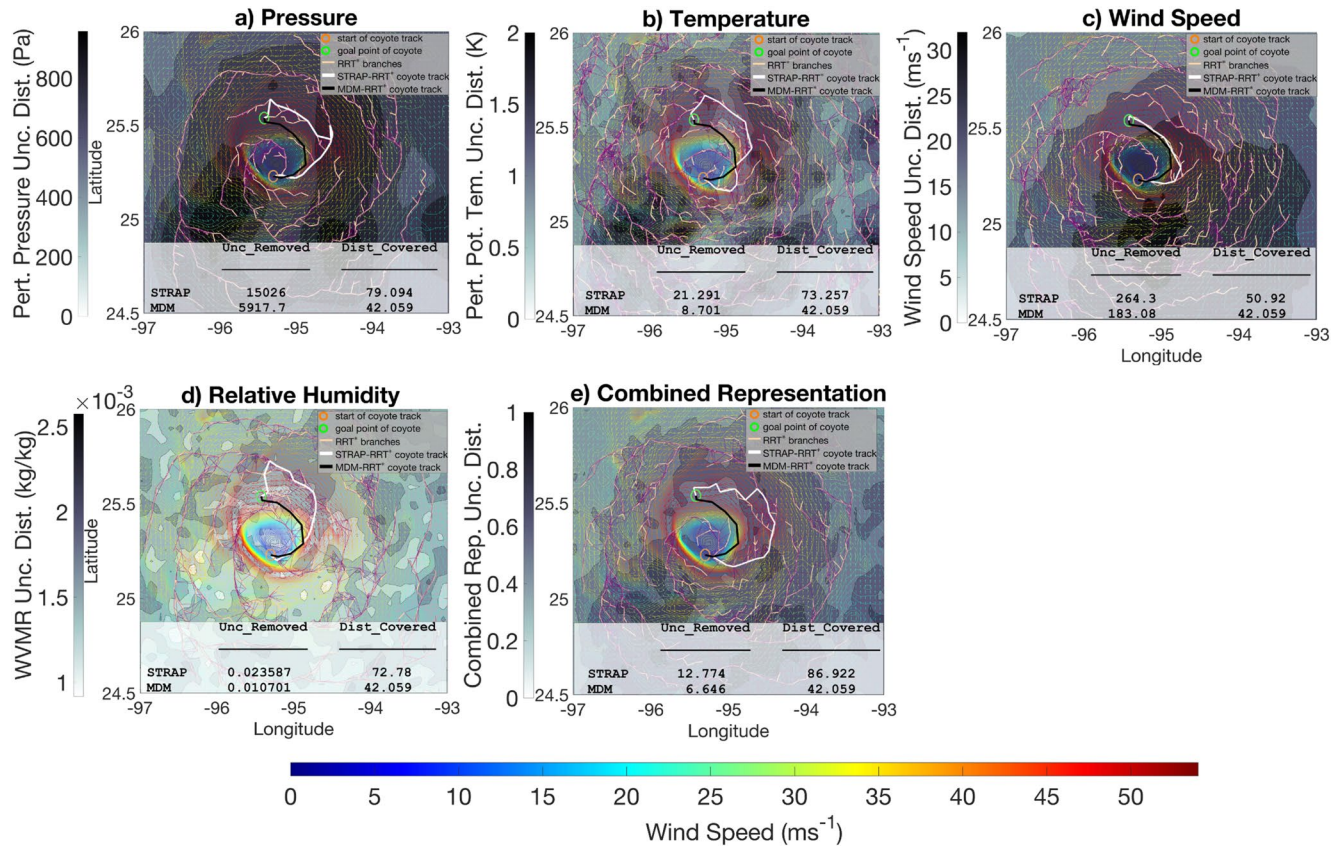
Figure 3. Storm-centered horizontal cross sections are shown at a 1.1-km level for standard deviation (underlying gray shading) for four variables (a–d) and a combined representation (e) overlaid with wind speeds vectored at 5 m s^{-1} intervals. The standard deviations are shaded in increments of 200 Pa for pressure, 0.5 K for temperature, 5 m s^{-1} for wind speed, 0.005 kg kg^{-1} for relative humidity and 0.1 for combined representation on 00:00 UTC August 25. *WVMR: Water Vapor Mixing Ratio. Symbol 🌀 represents the center of the hurricane.

by using the proposed method against the benchmark. We have tested all the different time windows and 00:00 UTC August 25 window showed the highest performance improvement following the nature of the uncertainty distribution at the inner-core. After multiple runs of STRAP-RRT* and MDM for different time windows, the average difference in uncertainty reduction between the two methods was very minimal. Those time windows usually had an almost uniform TC forecasting uncertainty at the inner-core region. Therefore, in such cases, the improvement of the proposed method may not be significant.

Figure 3 show degrees of uncertainties at different locations of the hurricane eye region as the underlying shading. We overlay the uncertainty distribution with the wind speed vectors to show the wind's direction and magnitude and important regions such as the eyewall. Figure 3a shows that the uncertainties of pressure have an overall-regular pattern at different regions of the inner-core. The uncertainties in these regions mostly decreased outwardly (max ≈ 900 Pa). Uncertainties of wind speed (Figure 3c) were significant (≈25 m s^{-1}) around the eyewall region, which usually translates to an increase in uncertainty of hurricane intensity forecast (e.g., wind speed at the radius of maximum wind) during this period. In general, the uncertainties of wind speed decreased outwardly, starting from a region close to the storm center and followed a mostly homogeneous and regular pattern similar to the uncertainties of pressure. This similarity may be due to the previously observed correlation between pressure and wind speed measurement (Rosendal & Shaw, 1982). Uncertainties of temperature and relative humidity (Figures 3b and 3d) were found to follow an irregular pattern. High temperature uncertainties (≈2 K) are also seen around the eyewall region. As noted in Rosendal and Shaw (1982), these high uncertainties are primarily due to large temperature gradients in the inner-core region. Likewise, we also observe high uncertainties (≈0.002 kg kg^{-1}) of relative humidity around the eyewall region. We observe similar high uncertainties around the eyewall region in the combined representation of the uncertainty for the four state variables. In many respects,

Figure 4. Safe and efficient Coyote path solution for STRAP-RRT* and MDM on storm-centered horizontal cross sections are shown at a 1.1-km level for standard deviation (underlying gray shading) of four variables (a–d) and a combined representation (e) overlaid with wind speeds vectored at 5 m s^{-1} intervals on 00:00 UTC August 25. *Purple lines in the RRT* solution connect neighboring nodes with maximum uncertainty to the tree, to find an alternate path. *Unc_Removed:* Uncertainty Removed, *Dist_Covered:* Distance Covered.

the nature of the uncertainty distribution of the combined representation is regular and homogeneous and similar to that of pressure and wind speed. Using the knowledge of the uncertainty distribution of the prior TC prediction, we can improve the posterior TC prediction by targeting the locations of high uncertainties.

4.2. Model Performance

The simulation results for STRAP-RRT* and MDM are first reported for a random start and goal location in the hurricane's inner-core region (within a radius of 57.539 miles from the center of the storm (Shea & Gray, 1973). Several studies have reported this region to provide data with the most significant impact on predictability of TCs (Cione et al., 2013, 2016; Emanuel & Zhang, 2017). For example, Emanuel and Zhang (2017) demonstrated that errors of inner-core moisture during initializations yield significant forecast errors.

The Coyote start location is at 25.23°N, 95.65°W, and the goal location is at 25.54°N, 95.71°W. Figure 4 shows the tree structure and the Coyote path solutions for STRAP-RRT* and MDM overlaid on the uncertainty distribution plots. Comparing the same number of observation points in each scenario, the path solution for STRAP-RRT* showed considerable potential in improving predictability of pressure measurements by selecting points of high uncertainties (Figure 4a). Specifically, the total uncertainty removed by STRAP-RRT* and MDM are 15,026 and 5917.7 Pa, which corresponds to improvement of over 150%.

As expected, the Coyote track distance for STRAP-RRT* was higher than MDM, with track distances 79.094 mi and 42.059 mi, respectively, corresponding to a 88% increase in distance for Coyote using STRAP-RRT*.

The findings in Figure 4b show significant potential in improving observation of temperature using STRAP-RRT*. When compared to MDM, there is an increase in total uncertainty removed from 8 to 21 K, representing
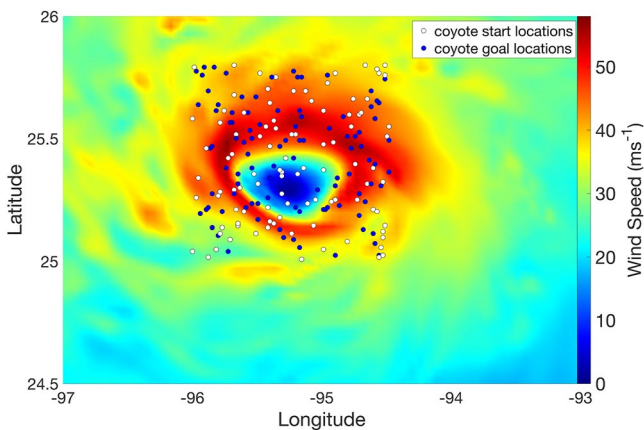
Figure 5. Distribution of 100 randomly sampled flight start and goal locations.

an improvement of over 160%. The increase in total uncertainty removed occurred at a 73% increase in Coyote track distance for STRAP-RRT*. Similarly, STRAP-RRT* performed better than MDM in removing wind speed uncertainty (Figure 4c). Higher uncertainty removal of wind speed was from 183 m s^{-1} for MDM to 264 m s^{-1} for STRAP-RRT*, representing a 44% increase. This improvement occurred at a 19% increase in Coyote track distance using STRAP-RRT*. Significant improvements ($\approx$130) is also estimated by removing uncertainties of relative humidity using STRAP-RRT* compared to MDM. This improvement occurred at a 71% increase in Coyote track distance using STRAP-RRT*.

STRAP-RRT* solutions on the combined representation of uncertainty distribution (Figure 4d) reported improvements of over 25% when compared to the MDM. This occurs at a 40% increase in Coyote sUAS track distance to the goal location. Overall, the performance of the model on individual uncertainty distribution tends to be similar to that of the combined representation. The tradeoff between total uncertainty removed and the total distance is reasonable, considering the algorithm allows the Coyote to minimize the energy utilized and increase range for navigation by using the wind velocity constraint.

4.3. Model Robustness Analysis

To assess the consistency and robustness in superior performance of the proposed model in various scenarios, STRAP-RRT* and MDM are compared over 100 scenarios of start and goal locations drawn from a uniform sample of locations around the eye region (Figure 5). The following notations identify the implementation results for each state variable: Pressure-STRAP (P_STRAP), Pressure-MDM (P_MDM), Temperature-STRAP (T_STRAP), Temperature-MDM (T_MDM), Wind speed-STRAP (W_STRAP), Wind speed-MDM (W_MDM), Combined representation-STRAP (C_STRAP), Relative Humidity-STRAP (RH_STRAP), Relative Humidity-MDM (RH_MDM), and Combined representation-MDM (C_MDM). The results of path solution (STRAP and MDM) for each scenario are reported considering the same number of observation points.

Figure 6 shows the performance of STRAP-RRT* compared to MDM for pressure uncertainty. Percentage increase is calculated as the change in computed value (total uncertainty and distance covered) for STRAP-RRT* relative to MDM. In general, the results indicate good performance for STRAP-RRT* in removing uncertainties, with improvements mostly ranging between 5% and 100%.

We mostly observe an increased Coyote track distance for STRAP-RRT* compared to MDM, ranging between 10% and 80%, although a few scenarios of STRAP-RRT* reported decreased flight distance than MDM.

Figure 7 shows the performance of STRAP-RRT* compared to MDM for temperature uncertainty. In most instances, it is seen that STRAP-RRT* resulted in significant improvement in removing uncertainty, with improvements ranging between 5% and 60%. STRAP-RRT* mostly resulted in increased Coyote track distances, although few scenarios reported lower track distances than MDM. A few of these scenarios still resulted in higher uncertainty removal than MDM. Overall, the increased Coyote track distance for STRAP-RRT* ranged between of 1% and 60%.

Figure 8 shows the performance of STRAP-RRT* compared to MDM for wind speed uncertainty. STRAP-RRT* results indicate a similar trend of good performance as seen above for pressure (Figure 6), although a few scenarios reported lower improvement levels. In general, the improvement in uncertainty removal ranged between 2% and 60%. A few scenarios reported a lower track distances for STRAP-RRT* but a higher uncertainty removal than MDM. Increases in Coyote track distance for STRAP-RRT* ranged between 1% and 62%.

Figure 9 shows the performance of STRAP-RRT* compared to MDM for relative humidity uncertainty. Similar to the results for temperature, STRAP-RRT* resulted in significant improvement in removing uncertainty, with improvements ranging between 2% and 50%. Generally, STRAP-RRT* resulted in increased Coyote track
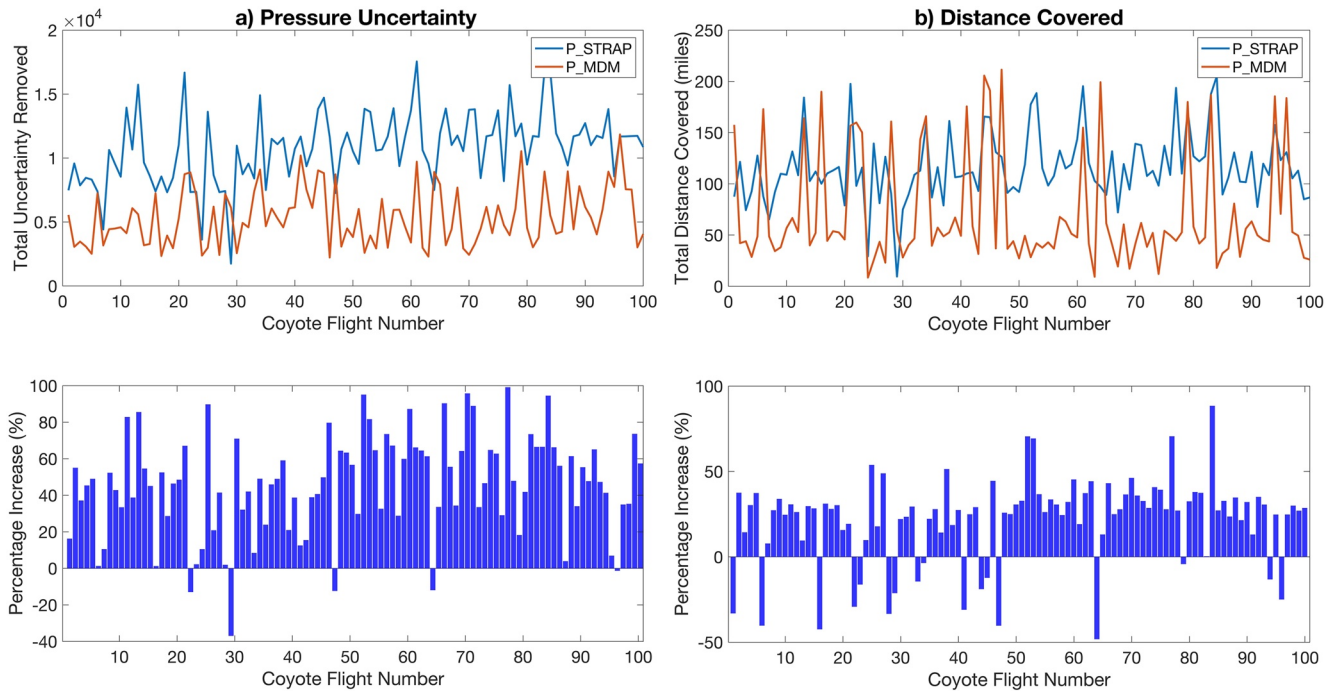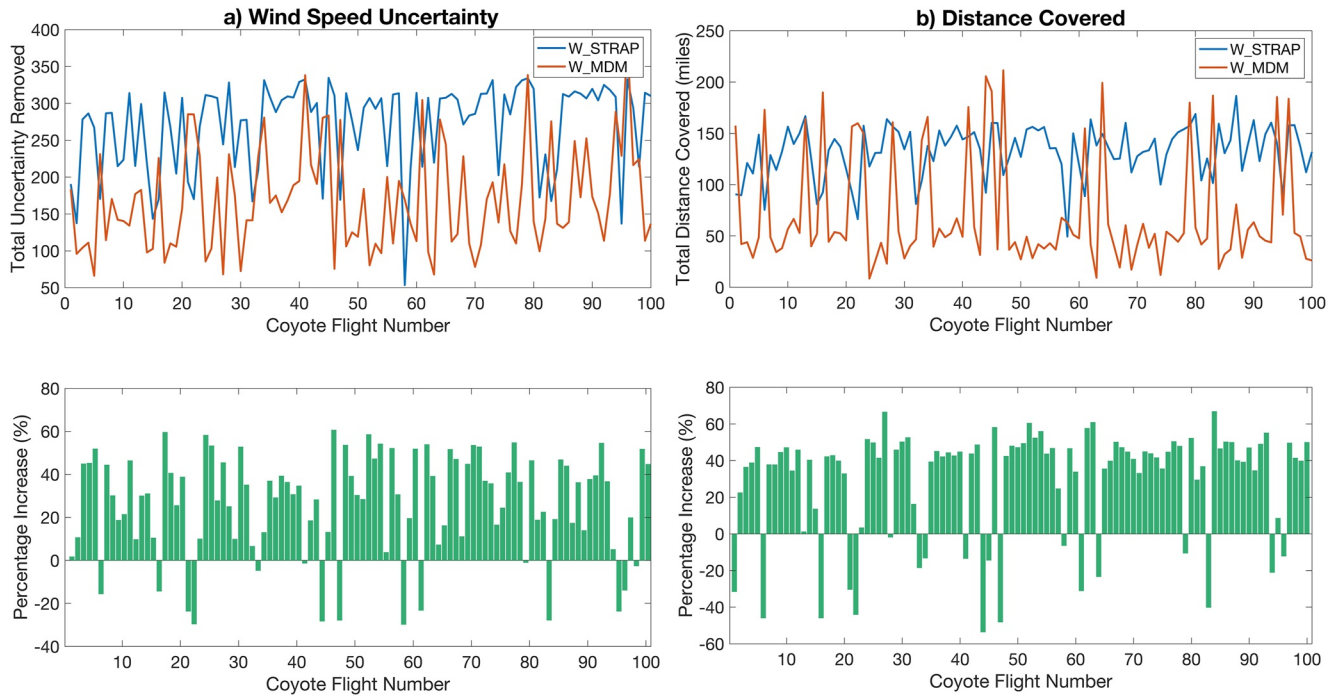
Figure 6. Pressure uncertainty analysis for P_STRAP and P_MDM.

distances, although few scenarios reported lower track distances than MDM. The increased Coyote track distance for STRAP-RRT* ranged between of 1% and 100%.

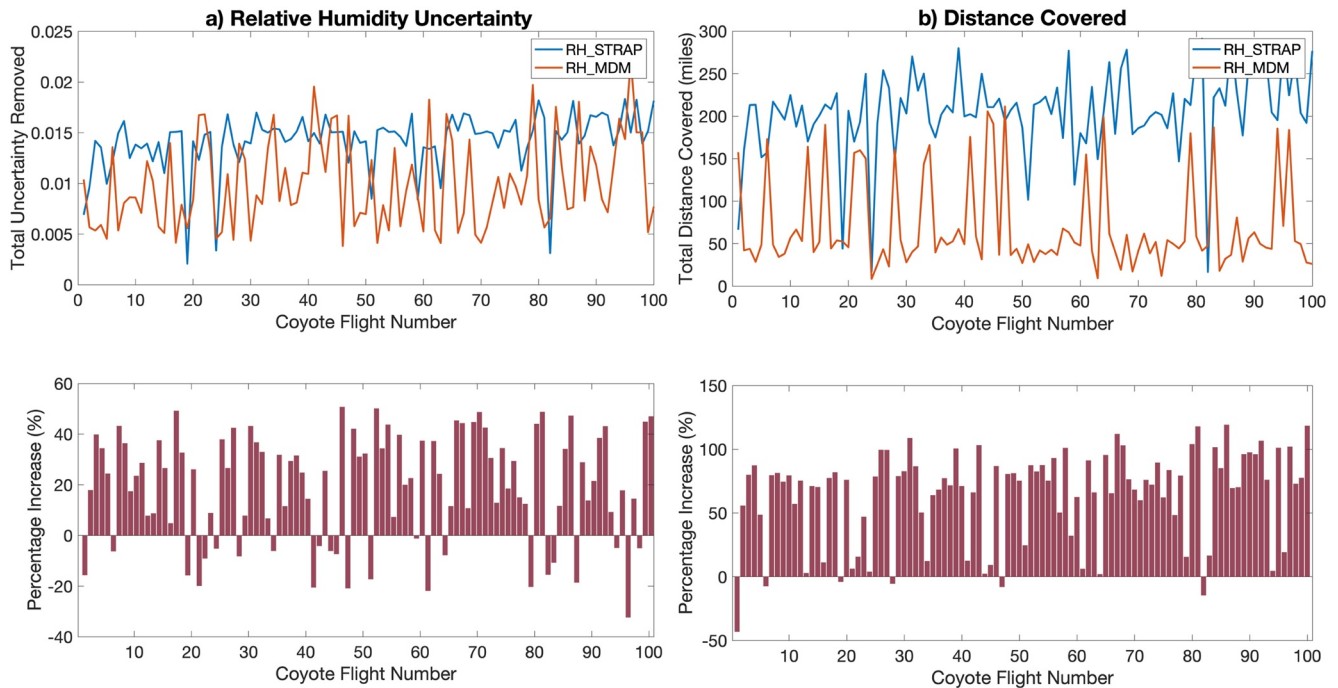Figure 10 shows the performance of STRAP-RRT* compared to MDM for the combined representation for uncertainty. Clearly, STRAP-RRT* results in significant improvements in the removal of uncertainty, with
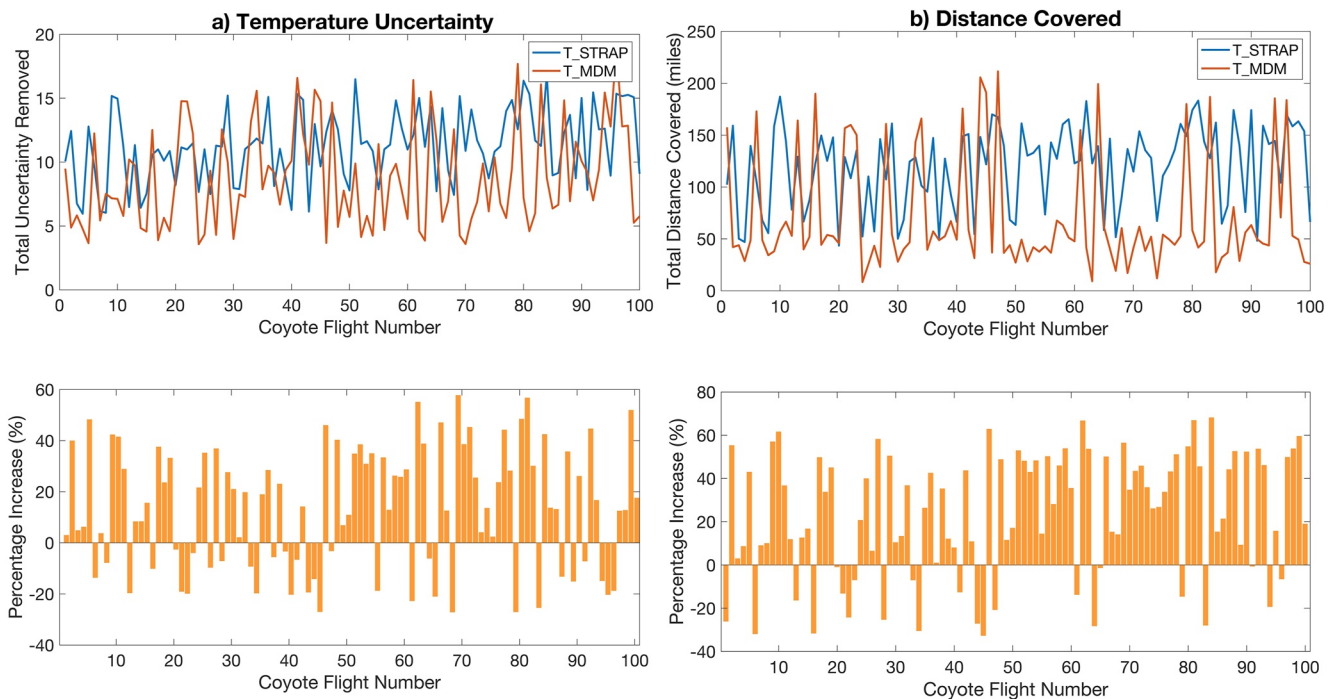
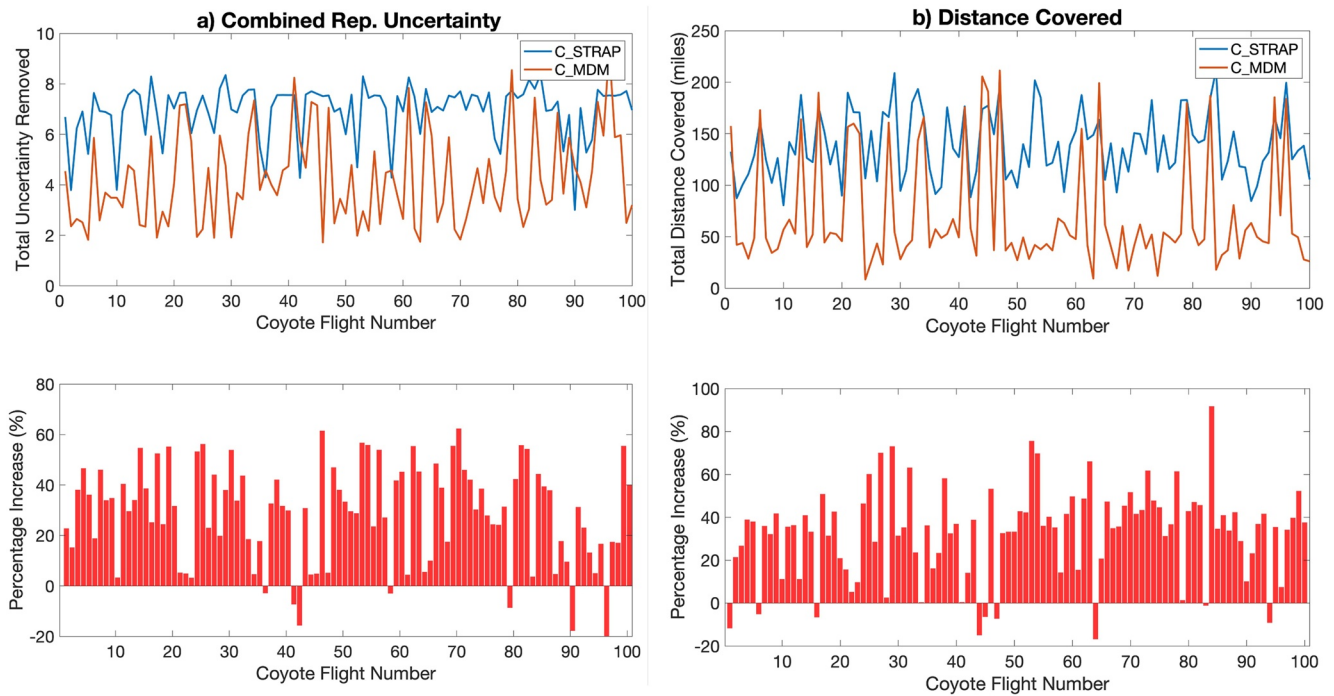

Figure 7. Temperature uncertainty analysis for T_STRAP and T_MDM.

Figure 8. Wind speed uncertainty analysis for W_STRAP and W_MDM.

Figure 9. Relative humidity uncertainty analysis for RH_STRAP and RH_MDM.

Figure 10. Combined representation uncertainty analysis for C_STRAP and C_MDM.

improvements mostly ranging between 5% and 75%. A few scenarios resulted in lower track distances for STRAP-RRT* than MDM, although a number these scenarios reported a higher uncertainty removal than MDM. The increased Coyote track distance for STRAP-RRT* ranged between 1% and 90%.

The parallel boxplots in Figure 11 illustrate the distribution of uncertainty removal and distance covered for the state variables for STRAP-RRT* and MDM. STRAP-RRT* distribution indicates good performance for removing uncertainty with few outliers. Interquartile ranges for uncertainty removal using STRAP-RRT* are typically higher than MDM. In all cases of uncertainty removal analysis, STRAP-RRT* reported a higher median than MDM. The uncertainty removal distribution for pressure and relative humidity had the highest number of outliers, while T_STRAP, T_MDM, C_MDM, and C_STRAP reported no outliers.

The distribution of total distance covered is as expected. Interquartile ranges for STRAP-RRT* are typically larger than MDM, indicating a higher overall flight distance. The distribution of Coyote flight distance for pressure and relative humidity observations has the highest number of outliers. Overall, the mean flight distance for Coyote flights using STRAP-RRT* was greater than MDM.

The findings of the Monte Carlo simulation suggest good performance for STRAP-RRT* in targeting locations of high uncertainties. This determination is mostly due in part to STRAP-RRT* evaluating the uncertainty of the prior forecasted measurement in deciding which location to visit. The implementation of STRAP-RRT* on the combined representation showed excellent performance, reporting no outliers for total uncertainties removed and distance covered.

This performance is especially significant since in situ observations of the different state variables are made simultaneously as the Coyote sUAS traverses a given path and therefore the actual benefit of STRAP-RRT* can be truly deduced from the analysis of the combined representation for uncertainty distribution. A significant resolution of uncertainties at the inner-core can therefore be achieved using STRAP-RRT*, which will result in an improved estimation of measurements in the inner-core structure.
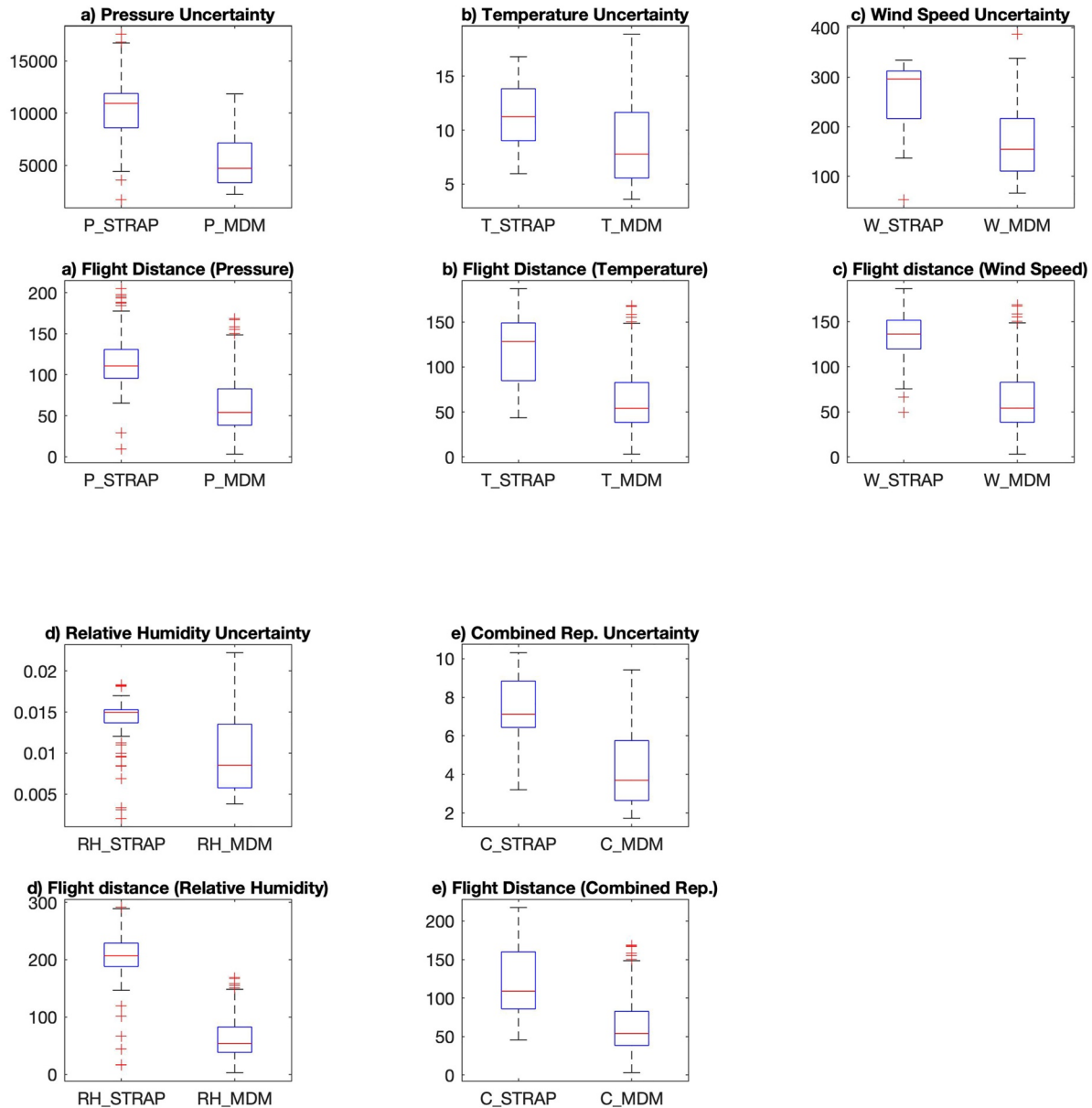
Figure 11. Summary statistics for total uncertainty removed and distance covered for 100 Coyote flights.

5. Data Assimilation

The relative significance of the improvement achieved by removing uncertainty can be assessed through a data assimilation analysis. Data assimilation adjusts the measurements of the state variables (temperature, pressure, wind speed, and relative humidity) directly during a period for which you want the estimates. We perform preliminary data assimilation analysis equivalent to a simple scalar illustration of the least squares estimation for a typical Coyote sUAS mission using STRAP-RRT*

5.1. Merging sUAS Observations and Prior Model Data

The series of discrete point in situ observations by the sUAS is assimilated with the prior forecasted measurements of the TC to provide the best estimate (posterior) of the measurements for the TC structure. The measurements are univariate and represented as grid point values. Assume two observations given by:

Background information at location i:

$$M_{\mathrm{P}(x,i)} + \sigma^2_{\mathrm{P}(x,i)} \tag{6}$$

and after sUAS observation at location i:

$$M_{\mathrm{O}(x,i)} + \sigma^2_{\mathrm{O}(x,i)} \tag{7}$$

where $M_{\mathrm{P}(x,i)}$ is the prior forecasted measurement at location i, $\sigma^2_{\mathrm{P}(x,i)}$ is the variance of forecasted measurement at location i, $M_{\mathrm{O}(x,i)}$ is the sUAS observation at location i, $\sigma^2_{\mathrm{O}(x,i)}$ variance of sUAS observation at location i. The variance $\sigma^2_{\mathrm{O}(x,i)}$ represents the imperfections of observations made by sUAS sensors. For scenarios where observations are treated as excellent, the data assimilation method will replace the forecasted measurement at the location with the observation. Observations are far from perfect due to sensor limitations; therefore, assimilation is usually carried out through a weighted estimate of forecasted measurement and observation based on their respective variance. The best estimate of the measurement of variable x at location i is written as:

$$M_{\mathbf{bestestimate}(x,i)} = (1 - \beta_{(x,i)})M_{\mathrm{P}(x,i)} + \beta_{(x,i)}M_{\mathrm{O}(x,i)} \tag{8}$$

$\beta_{(x,i)}$ is the weight between the forecasted measurement and observation. The best estimate of weight considers the variance of forecasted measurement and observation, written as:

$$\beta_{(x,i)} = \frac{\sigma^2_{\mathrm{P}(x,i)}}{\sigma^2_{\mathrm{P}(x,i)} + \sigma^2_{\mathrm{O}(x,i)}}. \tag{9}$$

The variance of the best estimate of measurement for variable x at location i is less than that of either the prediction or the observation written as:

$$\sigma^2_{\mathbf{bestestimate}(x,i)} = (1 - \beta_{(x,i)})\sigma^2_{\mathrm{P}(x,i)} \tag{10}$$

To account for the effect of an influence region around each observation point, we introduce a weighting function $\omega(i, j)$, to update the best estimates of the variance at each grid locations j in the vicinity of observation point i written as:

$$\omega(i, j) = \max\left(0, \frac{R^2 - d^2_{i,j}}{R^2 + d^2_{i,j}}\right) \tag{11}$$

where $d_{i,j}$ is a measure of the distance between points i and j. The weighting function $\omega(i, j)$ equals to one if the grid point j is collocated with observation i. It is a deceasing function of distance which is zero if $d_{i,j} \geq R$. R ("the influence region or radius") is a user defined constant beyond which the observations have no weight. In this analysis, we assume β from Equation 9 is directly related to the accuracy of the instrument making the observation. The modified best estimate of the variance at each grid point location j can now be written as:

$$\sigma^2_{\mathbf{bestestimate}(x,j)} = (1 - \beta_{(x,i)} * \omega(i, j))\sigma^2_{\mathrm{P}(x,j)} \tag{12}$$

5.2. Data Assimilation Analysis

This section illustrates the resulting improvements from a Coyote sUAS mission in a TC using the proposed deployment scheme. The analysis is carried out using the combined representation of uncertainty distribution from previous section. Although we will consider spatial correlation in the future, we still show promising improvements based on proposed methods. For each sample observation made by the Coyote sUAS, we specify a constant influence region ($R = 6$ mi) around the observation location. The mission starts with a fixed dropoff location at 25.5495°N, 94.4398°W and a randomly sampled without replacement multiple-goal locations. The energy-efficient navigation Coyote flight considering endurance, shows total distance in the range greater than 70 mi but less or equal 105 mi. The goal location of a previous flight is set to be the start location of the next flight. After Coyote finds a goal location, we update the uncertainty distribution to reflect the new distribution resulting from

Table 2
Summary of Percentage Improvement in Simulation Model for Hurricane Harvey After Data Assimilation Using STRAP-RRT*

	Destination		% Improvement			
Distance covered (mi)	Latitude	Longitude	Pressure	Temperature	Wind speed	Relative humidity
75.731	25.807	−94.801	3.133	1.921	2.816	1.057
83.984	25.207	−95.480	3.806	1.510	2.947	1.002
86.984	25.194	−95.008	4.054	1.957	3.370	1.050
96.093	25.064	−94.623	3.598	1.430	2.909	1.031
101.005	25.103	−94.512	3.440	1.401	2.744	1.231

our previous observation. We assume a uniformly distributed β between 0.8 and 0.9 (given that observations are at least 80% more important than the simulation model but less than 90% important than the forecasted measurement) at different locations in the TC space.

Table 2 shows the results of improvement in the estimates of the TC forecasting. Improvement in TC estimates is calculated as the difference between the sum of TC variances before and after Coyote flight data assimilation. Improvement in the measurement of pressure and wind speed was relatively high and similar in trend. This can mainly be due to the similarities in the uncertainty distribution for these two state variables. Temperature and relative humidity reported the lowest percentage improvement, mainly due to the very sparse and irregular distribution of uncertainty. Note that the results are the improvements for the entire TC structure and thus underestimate actual improvement for the inner-core region.

In general, the analysis indicates the Coyote sUAS mission with goal destination 25.194°N, 95.008°W would have resulted in the most improvement in the estimates of the TC structure. However, the distance covered in this mission is relatively smaller when compared to the last two missions in Table 2.

Figure 12 show that the data assimilation process for the scenario with the most improvement without considering the spatial correlation. Note that uncertainty distribution values along the recommended path of the Coyote sUAS are almost reduced to zero. Because we use the combined representation of the uncertainties as background information for STRAP-RRT*, the optimal path is from the contributing effect of the four variables at each location in the TC space. Therefore, the path may be biased depending on the value of each state variable's uncertainties at a location. Comparing the uncertainties of the storm structure before (Figure 12a) and after (Figure 12b) data assimilation of simulated Coyote sUAS observations, the optimal path targeted the uncertainties found mainly in the region of the eyewall. Specifically, the in situ sUAS observations will significantly reduce the estimated uncertainties of the forecasted measurement of pressure, temperature, wind speed, and relative humidity in this region. Focusing on the uncertainties of wind speed before (Figure 12c) and after (Figure 12d) data assimilation, we see that this simulated sUAS optimal path is in the vicinity of the radius of maximum winds (RMW). Specifically looking at Figure 12e, representing the forecasted wind speeds, we see that RMW is found in the wind flow circulations around 25.5°N in the horizontal cross sections of Hurricane Harvey at 00:00 UTC August 25. This suggests a reduction in the uncertainty of the estimated maximum sustained wind speed (intensity) at the time. In other words, assimilation of the simulated Coyote flight data reduced average wind speed variances in the vicinity of the RMW. Finally, because Hurricane Harvey was in the process of undergoing rapid intensification at 00:00 UTC August 25, there was more improvement in TC forecasting at this time. This new measurement will provide a more accurate initial state and will likely improve the predictability of rapid intensification for the near future state.

6. Conclusion

This study presents a sampling-based path planning algorithm to optimally sample observations that yield the most informative measurements with lower risk through uncertainty removal under turbulent flow. In order to minimize the energy utilized for navigation, a wind velocity constraint is implemented as an acceptable angular difference between a subpath segment and the wind velocity allowing the sUAS to mostly follow the strong TCs
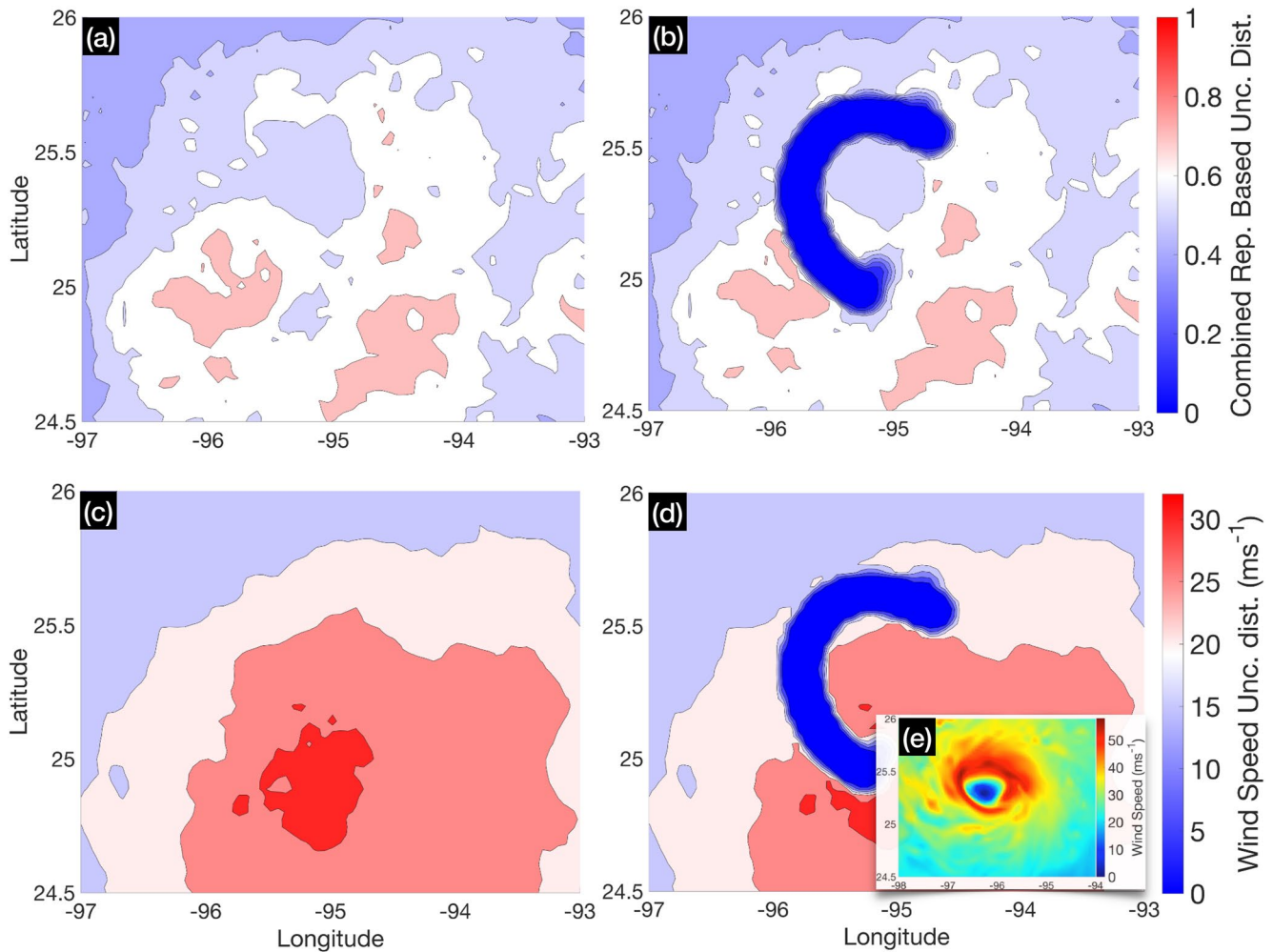
Figure 12. Illustrative data assimilation process for optimal Coyote flight mission using STRAP-RRT*; Before (a) and after (b) assimilation of Coyote flight data for uncertainties of the combined representation, before (c) and after (d) assimilation of Coyote flight data for uncertainties of wind speed. Also shown is the forecasted measurement of wind speed (e) in the inner-core.

wind direction. The current study highlights a promising solution for sUAV navigation as they can fly into the targeted TC inner-core to obtain high-resolution meteorological observations guided by background estimates (e.g., ensemble spread) from an earlier data assimilation process. The new observations from the TC boundary layer (i.e., interface between the ocean and atmosphere) supplement existing partial knowledge (Cione et al., 2013) for a better estimate of TC intensity. Although we did not consider the spatial correlation in the TC structure, the results showed significant improvement in the accuracy of the TC structure after Coyote sUAS followed the recommended path from STRAP-RRT*.

In future research, a systematic investigation using a sensitivity map will be considered, incorporating the storm structure's spatiotemporal dependencies. A sensitivity map estimates the impact of potential future direct observation at a location on reducing the forecast error. While this study on optimal sampling for a single sUAS, future studies will focus on a multiagent sUAS collaborative framework to maximize benefits, sequentially or simultaneously lunched by P3 aircraft. Past TC missions have deployed multiple Coyote sUAS one at a time independently with only a limited area of coverage or point measurement. However, this scheme makes the monitoring difficult for different sections of the boundary layer, failing to utilize the collaborative framework. A previous decision of first location assignment of the Coyote sUAS could turn out to be not optimal, after computing the expected benefit of the second assignment of the Coyote sUAS. On the contrary, poor information gathered as a result of the first location assignment could have a cascading effect on the following Coyote sUAS

assignments. A myopic decision may focus more on information gain on the one Coyote sUAS assignment in the current stage, but if the next assignment location is too far, a relatively late arrival time could lower the chance of collecting critical data in the second stage since the TC has already moved. Potential candidate for multiagent optimization includes the distributed constraint optimization (Darko et al., 2021) to coordinate multiple sUAS platforms to maximize the sum of the resulting benefits by optimizing a launch location (start) and a route to the target location (goal) for each sUAS.

Data Availability Statement

The data used for these analyses are available at: https://figshare.com/s/90f31f60e5821dae90bd.

References

Cione, J. J., Bryan, G. H., Dobosy, R., Zhang, J. A., de Boer, G., Aksoy, A., et al. (2020). Eye of the storm: Observing hurricanes with a small unmanned aircraft system. *Bulletin of the American Meteorological Society*, *101*(2), E186–E205. https://doi.org/10.1175/bams-d-19-0169.1

Cione, J. J., Kalina, E., Uhlhorn, E., Farber, A., & Damiano, B. (2016). Coyote unmanned aircraft system observations in Hurricane Edouard (2014). *Earth and Space Science*, *3*, 370–380. https://doi.org/10.1002/2016EA000187

Cione, J. J., Kalina, E. A., Zhang, J. A., & Uhlhorn, E. W. (2013). Observations of air–sea interaction and intensity change in hurricanes. *Monthly Weather Review*, *141*(7), 2368–2382. https://doi.org/10.1175/mwr-d-12-00070.1

Darko, J., Folsom, L., Deshpande, N., & Park, H. (2021). Distributed constraint optimization problem for coordinated response of unmanned aerial vehicles and ground vehicles. In *2021 55th annual conference on information sciences and systems (CISS)* (pp. 1–6). https://doi.org/10.1109/ciss50987.2021.9400249

de Boer, G., Argrow, B., Cassano, J., Cione, J., Frew, E., Lawrence, D., et al. (2019). Advancing unmanned aerial capabilities for atmospheric research. *Bulletin of the American Meteorological Society*, *100*(3), ES105–ES108. https://doi.org/10.1175/bams-d-18-0254.1

DeMaria, M., & Kaplan, J. (1999). An updated statistical hurricane intensity prediction scheme (ships) for the Atlantic and eastern north pacific basins. *Weather and Forecasting*, *14*(3), 326–337. https://doi.org/10.1175/1520-0434(1999)014<0326:AUSHIP>2.0.CO;2

DeMaria, M., Mainelli, M., Shay, L. K., Knaff, J. A., & Kaplan, J. (2005). Further improvements to the statistical hurricane intensity prediction scheme (ships). *Weather and Forecasting*, *20*(4), 531–543. https://doi.org/10.1175/waf862.1

DeMaria, M., Sampson, C. R., Knaff, J. A., & Musgrave, K. D. (2014). Is tropical cyclone intensity guidance improving? *Bulletin of the American Meteorological Society*, *95*(3), 387–398. https://doi.org/10.1175/bams-d-12-00240.1

Emanuel, K., & Zhang, F. (2017). The role of inner-core moisture in tropical cyclone predictability and practical forecast skill. *Journal of the Atmospheric Sciences*, *74*(7), 2315–2324. https://doi.org/10.1175/jas-d-17-0008.1

Folsom, L., Ono, M., Otsu, K., & Park, H. (2021). Scalable information-theoretic path planning for a rover-helicopter team in uncertain environments. *International Journal of Advanced Robotic Systems*, *18*(2), 1729881421999587. https://doi.org/10.1177/1729881421999587

Goyal, P. K., & Datta, T. (2011). Probability distributions for cyclone key parameters and cyclonic wind speed for the east coast of Indian region. *The International Journal of Ocean and Climate Systems*, *2*(3), 209–223. https://doi.org/10.1260/1759-3131.2.3.209

Malakar, P., Kesarkar, A. P., Bhate, J., & Deshamukhya, A. (2020). Appraisal of data assimilation techniques for dynamical downscaling of the structure and intensity of tropical cyclones. *Earth and Space Science*, *7*, e2019EA000945. https://doi.org/10.1029/2019EA000945

Minamide, M., Zhang, F., & Clothiaux, E. E. (2020). Nonlinear forecast error growth of rapidly intensifying Hurricane Harvey (2017) examined through convection-permitting ensemble assimilation of goes-16 all-sky radiances. *Journal of the Atmospheric Sciences*, *77*(12), 4277–4296. https://doi.org/10.1175/jas-d-19-0279.1

Munsell, E. B., Zhang, F., & Stern, D. P. (2013). Predictability and dynamics of a nonintensifying tropical storm: Erika (2009). *Journal of the Atmospheric Sciences*, *70*(8), 2505–2524. https://doi.org/10.1175/jas-d-12-0243.1

Pillar-Little, G. B. R., Elizabeth, A., Lappin, F. M., Bell, T. M., Segales, A. R., de Azevedo, G. B. H., et al. (2020). Observations of the thermodynamic and kinematic state of the atmospheric boundary layer over the San Luis Valley, CO using remotely piloted aircraft systems during the lapse-rate field campaign. *Earth System Science Data Discussions*, *13*, 269–280. https://doi.org/10.5194/essd-13-269-2021

Poterjoy, J., & Zhang, F. (2011). Dynamics and structure of forecast error covariance in the core of a developing hurricane. *Journal of the Atmospheric Sciences*, *68*(8), 1586–1606. https://doi.org/10.1175/2011jas3681.1

Raavi, P. H., & Walsh, K. (2020). Sensitivity of tropical cyclone formation to resolution-dependent and independent tracking schemes in high-resolution climate model simulations. *Earth and Space Science*, *7*, e2019EA000906. https://doi.org/10.1029/2019EA000906

Rosendal, H. E., & Shaw, S. L. (1982). *Relationship of maximum sustained winds to minimum sea level pressure in central north pacific tropical cyclones* (NOAA Tech. Memo. NWSTM PR-24). U.S. Department of Commerce, National Oceanic and Atmospheric Administration, National Weather Service.

Sanabia, E. R., Barrett, B. S., Black, P. G., Chen, S., & Cummings, J. A. (2013). Real-time upper-ocean temperature observations from aircraft during operational hurricane reconnaissance missions: Axbt demonstration project year one results. *Weather and Forecasting*, *28*(6), 1404–1422. https://doi.org/10.1175/waf-d-12-00107.1

Shea, D. J., & Gray, W. M. (1973). The hurricane's inner core region. I. Symmetric and asymmetric structure. *Journal of the Atmospheric Sciences*, *30*(8), 1544–1564. https://doi.org/10.1175/1520-0469(1973)030<1544:THICRI>2.0.CO;2

Sippel, J. A., & Zhang, F. (2008). A probabilistic analysis of the dynamics and predictability of tropical cyclogenesis. *Journal of the Atmospheric Sciences*, *65*(11), 3440–3459. https://doi.org/10.1175/2008jas2597.1

Sippel, J. A., & Zhang, F. (2010). Factors affecting the predictability of hurricane humberto (2007). *Journal of the Atmospheric Sciences*, *67*(6), 1759–1778. https://doi.org/10.1175/2010jas3172.1

Stern, D. P., Bryan, G. H., & Aberson, S. D. (2016). Extreme low-level updrafts and wind speeds measured by Dropsondes in tropical cyclones. *Monthly Weather Review*, *144*(6), 2177–2204. https://doi.org/10.1175/mwr-d-15-0313.1

Tyrrell, G., & Holland, G. (2003). Continuous monitoring of the hurricane core: Availability of new long-endurance small drone aircraft. *Hurricane! Coping with Disaster: Progress and Challenges Since Galveston, 1900*, *55*, 291–304.

Van Sang, N., Smith, R. K., & Montgomery, M. T. (2008). Tropical-cyclone intensification and predictability in three dimensions. *Quarterly Journal of the Royal Meteorological Society*, *134*(632), 563–582. https://doi.org/10.1002/qj.235

Wu, Y., Shen, Z., & Tang, Y. (2020). A flow-dependent targeted observation method for ensemble Kalman filter assimilation systems. *Earth and Space Science*, *7*, e2020EA001149. doi.org/10.1029/2020EA001149

Zhang, F., Minamide, M., Nystrom, R. G., Chen, X., Lin, S.-J., & Harris, L. M. (2019). Improving Harvey forecasts with next-generation weather satellites: Advanced hurricane analysis and prediction with assimilation of goes-r all-sky radiances. *Bulletin of the American Meteorological Society*, *100*(7), 1217–1222. https://doi.org/10.1175/bams-d-18-0149.1

Zhang, J. A., & Cione, J. J. (2021). *Employing small unmanned aircraft systems to improve situational awareness and operational physical routines used to predict tropical cyclone structure and intensity*.

Zhang, J. A., Cione, J. J., Kalina, E. A., Uhlhorn, E. W., Hock, T., & Smith, J. A. (2017). Observations of infrared sea surface temperature and air–sea interaction in Hurricane Edouard (2014) using GPS Dropsondes. *Journal of Atmospheric and Oceanic Technology*, *34*(6), 1333–1349. https://doi.org/10.1175/jtech-d-16-0211.1